



# CHORUS

This is the accepted manuscript made available via CHORUS. The article has been published as:

## Direct measurement of electron channeling in a crystal using scanning transmission electron microscopy

L. Fitting Kourkoutis, M. K. Parker, V. Vaithyanathan, D. G. Schlom, and D. A. Muller

Phys. Rev. B **84**, 075485 — Published 17 August 2011

DOI: [10.1103/PhysRevB.84.075485](https://doi.org/10.1103/PhysRevB.84.075485)

# Direct measurement of electron channeling in a crystal using scanning transmission electron microscopy

L. Fitting Kourkoutis,<sup>1,\*</sup> M. K. Parker,<sup>1,†</sup> V. Vaithyanathan,<sup>2,‡</sup> D. G. Schlom,<sup>3</sup> and D. A. Muller<sup>1,4</sup>

<sup>1</sup>*School of Applied and Engineering Physics, Cornell University, Ithaca, NY 14853*

<sup>2</sup>*Department of Material Science and Engineering,  
Pennsylvania State University, University Park, PA 16802-5055, USA*

<sup>3</sup>*Department of Material Science and Engineering, Cornell University, Ithaca, NY 14853, USA*

<sup>4</sup>*Kavli Institute at Cornell for Nanoscale Science, Ithaca, NY 14853*

Self-focusing of an atomic-scale high-energy electron wave packet by channeling along a zone axis in crystalline silicon is directly measured by scanning transmission electron microscopy using thin epitaxial SrTiO<sub>3</sub>(100) islands grown on Si(100) as test objects. As the electron probe propagates down a silicon atom column it is progressively focused onto the column, resulting in a fourfold increase in the scattered signal at the channeling maximum. This results in an enhancement of the visibility of the SrTiO<sub>3</sub> islands, which is lost if the sample is flipped up-side-down and the channeling occurs only after the probe scatters off the SrTiO<sub>3</sub> layer. The evolution of the probe wavefunction calculated by the multislice method accurately predicts the trends in the channeling signal on an absolute thickness scale. We find that while electron channeling enhances the visibility of on-column atoms, it suppresses the contribution from off-column atoms. It can therefore be used as a filter to selectively image the atoms that are most aligned with the atomic columns of the substrate. Using this technique coherent islands can be distinguished from relaxed islands. For SrTiO<sub>3</sub> films formed in a topotactic reaction on Si(100) we show that only ~55% of the SrTiO<sub>3</sub> is aligned with the Si atom columns. The fraction of coherent SrTiO<sub>3</sub> islands on Si(100) can be increased by choosing growth conditions away from equilibrium.

## I. INTRODUCTION

Annular dark field (ADF) imaging in a scanning transmission electron microscope (STEM) has proven to be a powerful technique for characterizing buried structures, such as thin films, isolated vacancies and defects in a crystal<sup>1-4</sup>. Because the scattering contrast in high-angle annular dark field (HAADF) imaging is strongly dependent on the atomic number  $Z$ , it is often referred to as  $Z$ -contrast imaging<sup>5,6</sup>. In zone-oriented crystals, however, electron channeling causes the probe wavefunction to be focused on the atomic columns and can therefore greatly affect the ADF image contrast. Theoretical studies of electron channeling in crystals have shown that the probe intensity at the exit surface of a crystal can strongly be enhanced<sup>7-9</sup>, thus leading to increased visibility of an adatom<sup>8</sup> or of dopant atoms<sup>10</sup>.

Electron channeling through the substrate can also be used to image thin, buried layers, which we have previously shown in the case of SrTiO<sub>3</sub>(100) grown epitaxially on Si(100)<sup>11</sup>. Figures 1(a) and (b) show plan-view ADF-STEM images of a nominally 2.5 unit cell (uc) thick, buried SrTiO<sub>3</sub> layer. To exploit electron channeling the sample was oriented so that the electron probe has to propagate through the Si substrate before reaching the SrTiO<sub>3</sub> layer. By slowly moving along the wedge-shaped electron transparent sample, the thickness of the Si substrate was carefully tuned to maximize the contrast of the SrTiO<sub>3</sub> film. This allows the thin SrTiO<sub>3</sub> layer to be imaged and reveals that the film is not uniform, but forms islands. The higher magnification image (Fig. 1(b)) shows perovskite lattice fringes in the bright regions, confirming that these patches are due to SrTiO<sub>3</sub>.

At a compressive strain of ~1.7% for epitaxial SrTiO<sub>3</sub>/Si the nominal SrTiO<sub>3</sub> layer thickness of 2.5 unit cells is below the equilibrium critical thickness, above which the film becomes unstable to relaxation. In fully relaxed structures misfit dislocations are expected every 59 unit cells (~23 nm), and at lower densities in partially relaxed structures. The typical island size of 5-10 nm is much smaller than this length scale. We also do not see evidence for misfit dislocations in these thin films; neither in plan-view nor in cross-section (in contrast to thicker films, where we do). The formation of islands is therefore not driven by misfit strain. Instead, we have shown that the dewetting of thin SrTiO<sub>3</sub> grown on Si(100) is caused by a phase-separation instability<sup>11</sup>.

While experimentally, electron channeling has successfully been exploited to image buried structures, the channeling signal has so far not been measured directly, but rather simulations have been used to predict its evolution with crystal thickness.

Here, we directly measure channeling enhancement in Si(100) by using the ultrathin, buried SrTiO<sub>3</sub> islands as test objects to track the evolution of the differential ADF signal and find good agreement with simulations.

## II. METHODS

### A. Experimental

The SrTiO<sub>3</sub>/Si sample was prepared by molecular-beam epitaxy using the following growth sequence. First, a 1/2 monolayer (ML) Sr template<sup>12-15</sup> is deposited on a (2x1) reconstructed clean Si (001) surface at 700°C. After

cooling to close to room temperature, 3 MLs of epitaxial SrO followed by 2 MLs of amorphous TiO<sub>2</sub> are deposited in high oxygen partial pressures and then heated up in vacuum until the TiO<sub>2</sub> reacts (a topotactic reaction) with the underlying SrO to form SrTiO<sub>3</sub><sup>13,16</sup>. Finally, the film was capped with amorphous Si (a-Si) to prevent damage of the thin SrTiO<sub>3</sub> layer during the TEM sample preparation. In addition, a second sample was prepared as above, but with the thickness of the Sr template increased to 1 ML.

Cross-sectional and plan-view TEM samples were prepared by conventional tripod polishing followed by low-energy, low-angle ion milling in a Fischione Model 1010 ion mill. To minimize any water exposure, an alcohol based lubricant (Allied Blue Lube) was used during sample cutting and polishing. The plan-view sample was prepared by polishing the Si substrate at a 2° wedge angle and subsequent ion milling from the back side (substrate side).

Annular dark field (ADF) imaging was performed in a 200 kV FEI Tecnai F20 SuperTWIN STEM with a convergence semi-angle of  $(9.5 \pm 0.5)$  mrad. By varying the inner detector angle from  $\sim 65$  to  $\sim 22$  mrad, the imaging conditions can be switched from high-angle annular dark field (HAADF) to low-angle annular dark field (LAADF).

To increase the signal to noise ratio and average out the scan noise in the high-magnification images, Fig. 1(b) and (c), 7 and 11 successive images were cross-correlated and averaged in the two respective cases. Subsequently, the  $1024 \times 1024$  pixel images were rebinned to  $512 \times 512$  pixels.

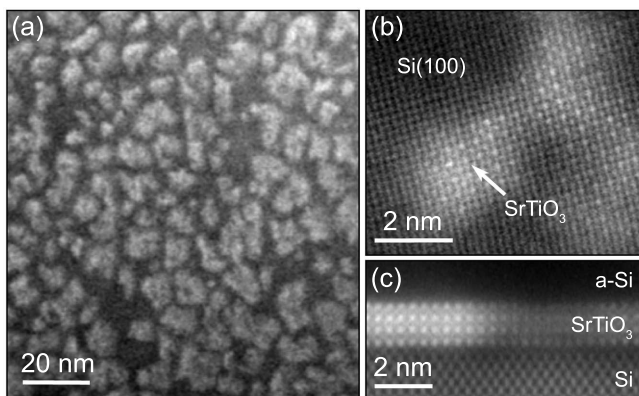


FIG. 1: (a), (b) Plan-view and (c) cross-sectional ADF-STEM images of a nominally 2.5  $\mu\text{c}$  thick epitaxial SrTiO<sub>3</sub>(100) film grown on Si(100) and capped with 15 nm of amorphous Si showing the formation of SrTiO<sub>3</sub> islands and nonuniform coverage. (a) and (b) are viewed along a substrate  $\langle 001 \rangle$  zone axis and (c) along a  $\langle 110 \rangle$  zone axis. For more details see Ref. 11.

## B. Simulations

Electron channeling, convergent beam electron diffraction (CBED) and ADF-STEM imaging were simulated using the multislice method<sup>6,18–20</sup> in which the specimen is divided into slices parallel to the optical axis of the microscope (typically a single slice corresponds to one atomic layer) separated by vacuum. For each slice the projected atomic potential and the transmission function, which ultimately produces a small phase shift in the electron wavefunction as it passes through the slice, are calculated. Starting with a probe wavefunction focused at a specific position on the specimen (in STEM), the wavefunction is transmitted through the sample, slice by slice, with Fresnel diffraction between slices. After propagating through the entire thickness of the crystal the electron wavefunction is diffracted onto the detector. The ADF intensity is computed by incoherently integrating the intensity of the diffracted wavefunction over the annular detector geometry. The multislice calculation is then repeated for each position of the incident focused electron probe.

Phonon scattering is modeled using the frozen-phonon approximation<sup>21–23</sup> which assumes that the electron/atom interaction occurs so rapidly that the atom appears stationary and is frozen in “mid-vibration”<sup>21</sup>. Following the Einstein model for thermal vibrations the frequency of oscillation of each atom is taken to be constant and all the atomic displacements to be uncorrelated with each other. This results in a Gaussian probability distribution of the atomic displacements, where the standard deviation is the r.m.s. atomic displacement along each direction. Note that small displacements (i.e., subslice) along the optic axis (z-axis) are lost because only the projection of the atomic potentials along the z-axis is used to compute the slice transmission function. A single phonon configuration is then defined as the entire set of all random atomic displacements<sup>21</sup>. Finally, multislice calculations are performed for a series of phonon configurations and the results are averaged incoherently.

For comparison with experiment, the incident probe was modeled according to the conditions of a 200 kV FEI Tecnai F20 SuperTWIN STEM (spherical aberration coefficient ( $C_s$ ) = 1.2 mm, defocus ( $\Delta f$ ) = 450 Å, semi-angle of the probe forming aperture ( $\alpha_{ap}$ ) = 9.6 mrad). The evolution of the electron probe, initially placed on an atomic column at the center of a  $32.58 \times 32.58 \text{ \AA}^2$  ( $6 \times 6 \text{ uc}^2$ ) Si supercell and then propagating through the sample, was calculated on a  $1024 \times 1024$  pixel grid, allowing a maximum scattering angle of 263 mrad. Phonon scattering was taken into account as described above averaging over 20 phonon configurations with an r.m.s. atomic displacement for silicon of about  $0.078 \text{ \AA}$ <sup>24</sup>.

After propagation through the sample the exit wavefunction is diffracted, forming a CBED pattern. To obtain high resolution CBED patterns (high sampling in reciprocal space), a large supercell of  $108.6 \times 108.6 \text{ \AA}^2$  ( $20 \times 20 \text{ uc}^2$ ) was chosen. This results, for a  $1024 \times 1024$

pixel<sup>2</sup> grid, in a maximum scattering angle of  $\sim 79$  mrad, which is rather small since it does not include any higher-order Laue zone (HOLZ) rings. For our purposes, however, all features (scattering angles  $< 30$  mrad) were sufficiently reproduced, which we have confirmed by performing one calculation for a 22 nm thick crystal on a  $2048 \times 2048$  pixel<sup>2</sup> grid, which increases the maximum scattering angle to  $\sim 158$  mrad. Further care has to be taken when simulating CBED patterns with overlapping diffraction disks, as is the case for our imaging conditions. Phase information is included in the areas where diffraction disks overlap (interfere) and the contrast is therefore sensitive to the position of the electron probe if it is smaller than the unit cell size<sup>25</sup>. For larger electron probes the thickness of an on-axis crystal can be determined by matching experimental CBED patterns recorded with a stationary probe with simulated CBED patterns<sup>21,23,24</sup>. Alternatively, for finely focused probes similar results can be obtained by recording the position-averaged CBED pattern while scanning the beam across an area larger than a unit cell<sup>26,27</sup>. Accordingly, in the simulation of CBED patterns we have incoherently averaged CBED patterns for 36 positions in the unit cell. For each probe position the CBED patterns for 20 phonon configurations were averaged, i.e., the final CBED pattern at each thickness is an average over 720 individual CBED patterns. Finally, all simulated CBED patterns presented in this paper are displayed on the logarithmic scale to bring out the low-intensity features.

The channeling signal was determined by simulating the ADF intensity after each slice and taking the derivative with respect to the sample thickness. The atomic potentials and transmission functions were sampled on a  $4096 \times 4096$  pixel<sup>2</sup> grid over  $81.45 \times 81.45 \text{ \AA}^2$  ( $15 \times 15 \text{ uc}^2$ ), allowing a maximum scattering angle of  $\sim 420$  mrad and the signal was averaged over 20 phonon configurations. The ADF detector angles were set according to the experimental values, i.e., the inner detector angle is 65 mrad in HAADF and 22 mrad in LAADF and the outer angle is five times the inner angle.

The visibility of a single Sr atom on a Si crystal, discussed in section III C, was calculated using a  $2048 \times 2048$  pixel<sup>2</sup> grid over  $38.01 \times 38.01 \text{ \AA}^2$  ( $7 \times 7 \text{ uc}^2$ ), resulting in a maximum scattering angle of  $\sim 450$  mrad.

For all presented multislice results, except for the CBED calculations, the total integrated intensity after propagation of the wavefunction through the entire sample thickness is within 1 % of the incident intensity.

### III. RESULTS AND DISCUSSION

#### A. Multislice Simulations of electron channeling in Si(100)

The channeling signal, which is the differential ADF intensity  $dI/dz$  with  $z$  being the sample thickness, for

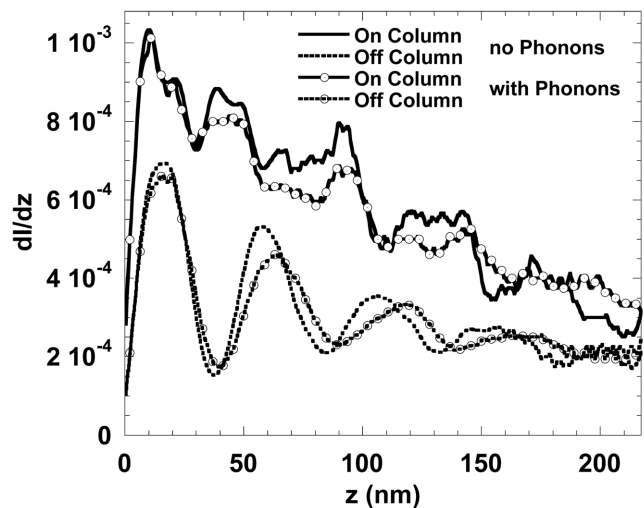


FIG. 2: Channeling signal,  $dI/dz$ , determined by simulating the ADF intensity after each slice and taking the derivative with respect to the sample thickness  $z$ . The channeling signal was computed for two probe positions, the first one on the atomic column and the second one in-between atomic columns, propagating down Si $\langle 001 \rangle$ . Phonon scattering was taken into account using the frozen-phonon approximation and following the Einstein model for thermal vibrations, averaging over 20 phonon configurations.

an electron probe propagating through a Si crystal along a  $\langle 001 \rangle$  axis is shown in Fig. 2. Within the first few nanometers  $dI/dz$  computed on an atomic column increases rapidly, reaching its maximum at  $\sim 10$  nm. The differential contribution to the ADF image intensity of an atom placed at the thickness of the channeling maximum is enhanced fourfold compared to that of an atom at the entrance surface of the crystal. The visibility of a thin, buried layer can therefore be maximized by selecting the thickness of the crystalline substrate to be close to the channeling maximum. Additionally, this effect is beneficial for ADF-STEM imaging of thin crystalline samples as it damps the contribution of the first few atomic layers, which are often damaged during the sample preparation process.

The effect of channeling can easily be understood in the framework of the linear-imaging model for ADF-STEM, which is valid for large ADF detector angles and states that the differential contribution to the ADF signal of a layer of atoms at thickness  $z$  is the convolution of the probe intensity  $|\Psi(\mathbf{r}_p, z)|^2$  and the object function  $T(\mathbf{r}, z)$  of that layer<sup>28</sup>. The final image intensity for a sample of thickness  $t$  is given by

$$I(\mathbf{r}_p) = \int_0^t |\Psi(\mathbf{r} - \mathbf{r}_p, z)|^2 \otimes T(\mathbf{r}, z) dz, \quad (1)$$

where  $\otimes$  stands for convolution. So, the differential contribution to the ADF signal is

$$\frac{dI}{dz}(\mathbf{r}_p, z) = |\Psi(\mathbf{r} - \mathbf{r}_p, z)|^2 \otimes T(\mathbf{r}, z). \quad (2)$$

When defining  $T(\mathbf{r}, z)$  as a set of delta functions at the atomic positions weighted by an atomic scattering strength, proportional to  $Z^{1.7}$  for ADF-STEM<sup>6,29</sup>, the channeling signal can be directly related to the probe intensity at thickness  $z$  via Eq. 2 as  $dI/dz \propto |\Psi(0, z)|^2$ , i.e., it tracks the on-column probe intensity.

The evolution of the electron probe shape as it propagates through the Si crystal was simulated using multislice. Within the first 10 nm the incident 1.4 Å beam is focused down to 0.5 Å, as shown in Fig. 3. At the channeling maximum the probe intensity is therefore strongly enhanced<sup>7-9</sup>, thus leading to increased visibility of an adatom<sup>8</sup> or a dopant atom at that thickness<sup>10</sup>.

After passing the first channeling maximum, the probe then dechannels, spreading intensity away from the center atomic column, which causes the channeling signal to drop to a minimum at  $z \sim 30$  nm. Some of the intensity then channels back to the atomic column, increasing  $dI/dz$  again. As the probe propagates further through the crystal, it continues to spread, resulting in an overall damping of the channeling signal.

Large changes in the channeling signal are observed as the probe is moved from an atomic column to in-between four atomic columns (Fig. 2). Here, the probe again channels over the first 10 nm after which it dechannels, resulting in a rapid decrease of  $dI/dz$ , almost down to the initial value at the sample entrance surface. At that point some of the probe intensity has channeled onto the atomic columns, resulting in a local maximum in the on-column channeling signal. For direct comparison with experimental results, phonon scattering has to be taken into account, which results in damping of some channeling peaks and for the off-column signal in a shift of the channeling peaks to larger thicknesses (Fig. 2).

Note, that in the case of Si(100) the interpretation of the channeling signal in the framework of the incoher-

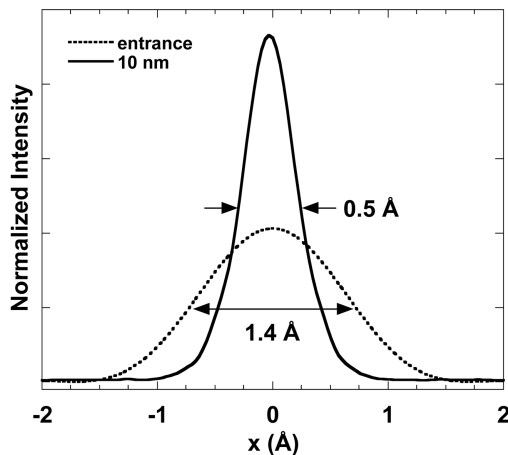


FIG. 3: Focusing of the electron probe in crystalline Si due to electron channeling along  $\langle 100 \rangle_{Si}$ . Probe profiles at the entrance and at the exit surface of a 10 nm thick Si crystal, respectively.

ent imaging model is valid only for thicknesses up to  $\sim 100$  nm. For larger thicknesses the proportionality of the channeling signal and the probe intensity (including the center and the neighboring columns) breaks down.

## B. Experimental results of electron channeling in Si(100)

The channeling signal at a specific thickness of the Si crystal can be directly determined from ADF images of the SrTiO<sub>3</sub>/Si sample discussed in Section I. The SrTiO<sub>3</sub> islands in different areas of the wedge-shaped sample are used in this case as test objects to track the evolution of the channeling signal with the thickness of the Si substrate.

Figure 4 (g-l) shows plan-view LAADF STEM images of SrTiO<sub>3</sub> islands on Si(100) in successively thicker parts of the sample, i.e., the average height of the SrTiO<sub>3</sub> islands remains constant, but the thickness of the Si substrate increases. For all displayed ADF images the difference between the maximum and the minimum intensity is fixed in order to demonstrate the change in the visibility of the SrTiO<sub>3</sub> islands. The thickness of the Si substrate was determined for each image from CBED patterns recorded while scanning the probe in the same area. By matching the experimental CBED patterns, shown in the left half of Fig. 4 (a-f), with simulated ones (right half of Fig. 4 (a-f)), the thickness of the Si substrate can be determined within  $\pm 2$  uc.

The procedure of extracting the average increase in the ADF image intensity due to the presence of the SrTiO<sub>3</sub> islands on the Si crystal from the experimental ADF images is demonstrated in Fig. 5. First, the background (Fig. 5(b)) of the original image (Fig. 5(a)) was removed using a singular value decomposition routine laid out by Voyles *et al.*<sup>10</sup>. The histogram of the resulting background subtracted image is then fitted by two Gaussians, one describing the regions of the sample that are covered by SrTiO<sub>3</sub> islands and the second describing the uncovered regions. The difference between the centers of the two Gaussians is the average increase of the ADF image intensity due to the presence of the SrTiO<sub>3</sub> on the Si substrate, and is therefore a measure of the channeling signal at the specific thickness of the Si crystal in that region.

After repeating the described procedure for each recorded image, the evolution of the ADF intensity of the SrTiO<sub>3</sub> islands, i.e., the channeling signal, with thickness can be determined. The open symbols in Fig. 6 show the experimentally determined channeling signal for the case that the crystalline substrate constitutes the entrance surface for the electron probe, which then channels in the crystal before reaching the SrTiO<sub>3</sub> layer. As expected from the multislice results (Fig. 2) the signal increases rapidly as the probe channels in the crystal, resulting in a fourfold increase in the differential ADF intensity from its initial value at zero thickness to its maximum at  $\sim 12$  nm.

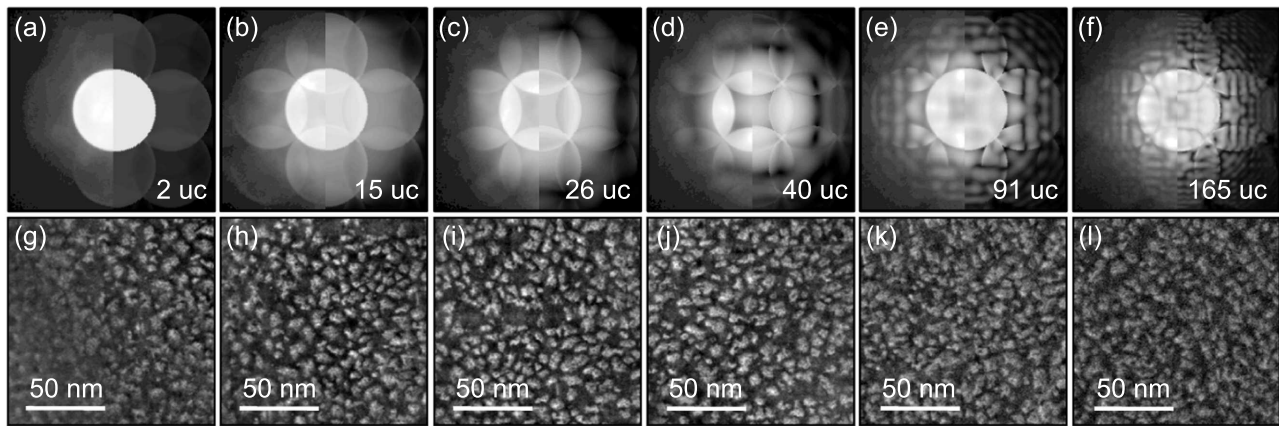


FIG. 4: Plan-view imaging of a thin epitaxial  $\text{SrTiO}_3$  film grown on crystalline Si and capped with amorphous Si in areas of the sample where the crystalline Si is increasingly thicker. The sample was oriented so that the electron probe first propagates through the crystalline Si substrate before reaching the  $\text{SrTiO}_3$  layer. The thickness of the crystal was determined by matching the experimentally recorded convergent beam electron diffraction (CBED) patterns (left half of (a-f)) with simulated CBED patterns of crystalline Si at various thicknesses (right half of (a-f)). Low angle annular dark field imaging of the epitaxial  $\text{SrTiO}_3$  film (g-l) reveal the change in the visibility of the  $\text{SrTiO}_3$  islands with sample thickness.

It then damps out for larger thicknesses. When directly comparing with the prediction, it is important to point out that experimentally the ADF intensity is averaged over all probe positions as the incident probe is scanned

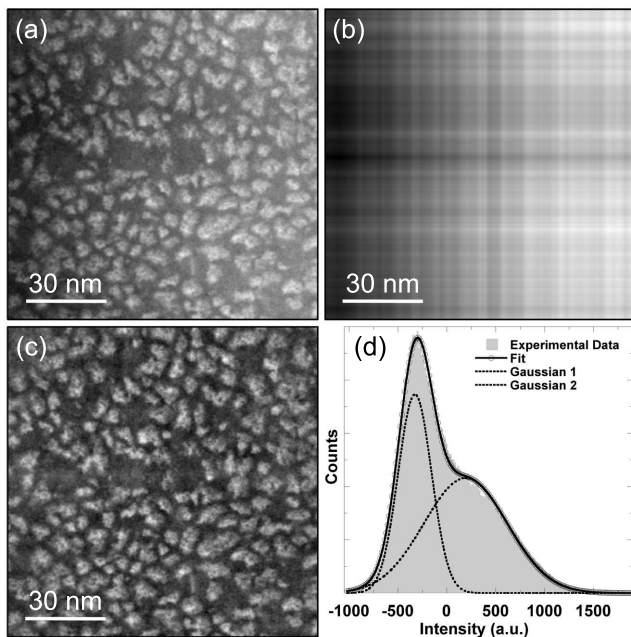


FIG. 5: Process of extracting the average ADF intensity of the  $\text{SrTiO}_3$  islands from plan-view ADF images. (a) Original ADF image, (b) background of (a) determined using a singular value decomposition routine and (c) the background subtracted image. The average intensity from the  $\text{SrTiO}_3$  islands is determined by fitting 2 Gaussians to the histogram of (c) and taking the difference between the centers of the two Gaussians.

across the area. For comparison with the experiment the simulated channeling signal is therefore approximated by the average of the channeling signal from on the atomic column and from in-between four atomic columns (both shown in Fig. 2). This simulated channeling signal is shown in Fig. 6 as a solid line. Note that not the absolute intensities, but only the qualitative behavior of the channeling signal is compared. Within the uncertainty of the experiment the theory matches our data, which demonstrated that this is, to the best of our knowledge, the first time that the evolution of the electron channeling signal in a crystal has directly been measured.

As a reality check the sample was then flipped up-side-down, so that the electron probe enters through the 15 nm thick amorphous Si capping layer, then reaches the  $\text{SrTiO}_3$  before propagating through the crystalline Si substrate. In this case, the probe does not undergo channeling before scattering off the  $\text{SrTiO}_3$  layer. Since the thickness of the a-Si layer is fixed for all areas on the sample where  $\text{SrTiO}_3$  islands are observed, the contribution to the ADF intensity from the  $\text{SrTiO}_3$  islands should remain constant. The solid symbols in Fig. 6 show the experimental results for this case and confirm this prediction. It is also worth pointing out that as the thickness of the crystalline Si approaches zero, the intensity of the  $\text{SrTiO}_3$  islands is about the same for both sample orientations, as channeling in the Si substrate is eliminated.

The difference in the differential contribution to the ADF intensity for the two sample orientations demonstrates how the visibility of an  $\text{SrTiO}_3$  island can be enhanced by exploiting electron channeling. Even for thicknesses larger than the optimum thickness, at which the channeling signal reaches its maximum, the intensity from the  $\text{SrTiO}_3$  islands is enhanced when the sample is oriented so that the probe channels in the crystalline

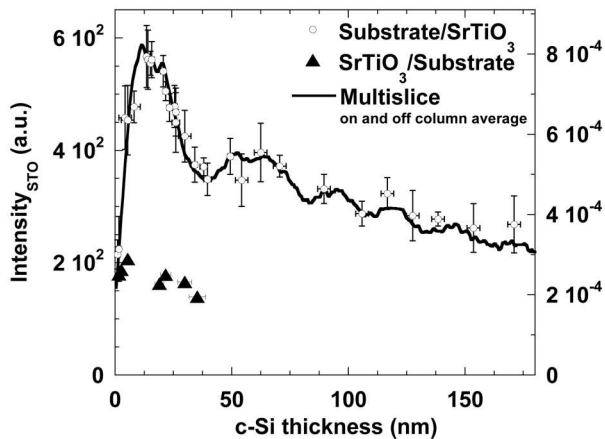


FIG. 6: Comparison of the theoretical and the experimentally measured channeling signal in Si(100). For the experimental results the orientation of the sample is labeled by Substrate/SrTiO<sub>3</sub>, when the electron probe propagates through the substrate before scattering off the SrTiO<sub>3</sub> layer and by SrTiO<sub>3</sub>/Substrate when the sample is flipped up-side-down. The error bars reflect the uncertainty in the determination of the crystal thickness by matching the experimental CBED patterns with simulations and the standard deviation of the intensity of the SrTiO<sub>3</sub> islands determined for different parts of the ADF image by the procedure described in the text.

substrate first.

Note that the presence of strain fields, which cause displacements from the expected crystal atomic sites<sup>30</sup>, can affect channeling of the electron probe and the ADF-STEM image contrast. Here, however, the center of the SrTiO<sub>3</sub> islands are fully strained according to the  $\sim 1.7\%$  lattice mismatch between Si and SrTiO<sub>3</sub><sup>11</sup>. The Sr atoms are therefore aligned with the Si columns and no additional contrast in the ADF image is expected.

### C. Electron channeling as a filter for on-column atoms

In the previous section we have experimentally shown that the visibility of a thin SrTiO<sub>3</sub> island can be enhanced by electron channeling in the substrate. As the probe channels onto the atomic column, its intensity and the differential contribution to the ADF signal increases. What happens, however, to an adatom that is displaced from the atomic column or is sitting in-between the atomic columns? In order to answer this question, we have calculated the visibility of a single Sr atom on Si(100) that is successively displaced from the atomic column. Here, the Sr visibility is defined as the fractional increase in the intensity due to the presence of the Sr atom.

Figure 7 shows the simulated Sr visibility as a Sr atom is displaced from the Si column along a  $\langle 100 \rangle_{Si}$  direction, as indicated in the sketch ( $\langle 110 \rangle_{Si}$  projection) in

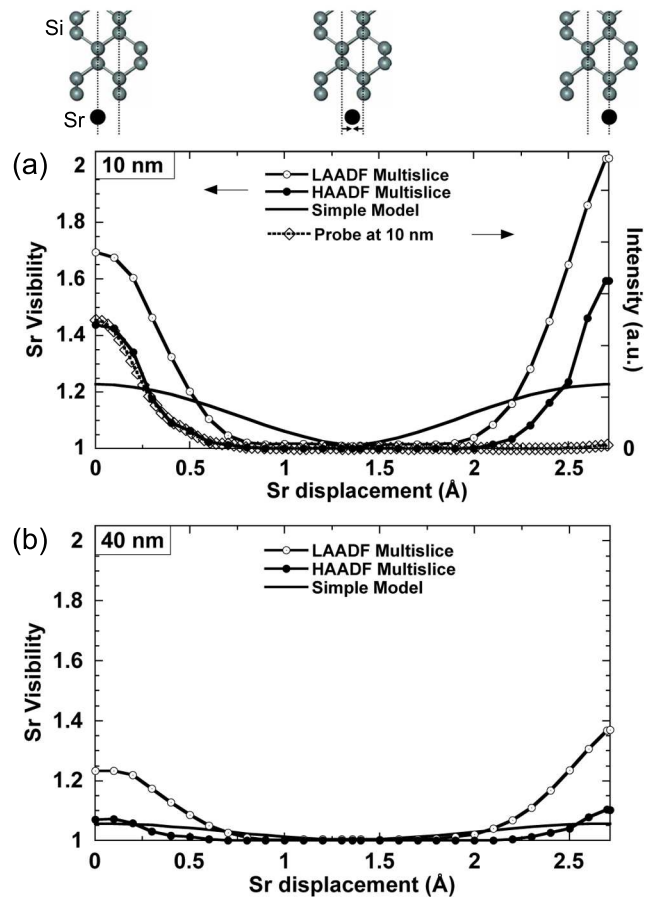


FIG. 7: Visibility of a single Sr atom placed on the side through which the electron beam exits of a (a) 10 nm and (b) 40 nm thick crystalline Si substrate. As the Sr atom is moved off an atomic column the visibility decreases and drops below the detection limit when displaced by less than 1 Å. The visibility is calculated using a simple model (convolution of the incident probe intensity with the projected position of all the atoms in the sample weighted by  $Z^{1.7}$ ) and multislice for two detector geometries corresponding to the LAADF and the HAADF signal. At a Si substrate thickness of 10 nm the Sr visibility for HAADF imaging closely follows the shape of the electron probe at that thickness.

the top panel. Two cases were simulated, one where the thickness of the Si crystal corresponds to the channeling maximum (10 nm) and one for a thicker Si crystal (40 nm). In both cases, the Sr visibility strongly depends on the position of the Sr atom. As the Sr atom is displaced from the Si atomic column the visibility decreases and eventually drops below the detection limit. The point at which it falls below the detection limit depends not only on the sample thickness, but also on the imaging condition. For a 10 nm thick Si crystal a single Sr atom disappears after being displaced by only  $\sim 0.5$  Å off the atomic column in HAADF imaging and by  $\sim 0.7$  Å in LAADF. As the thickness of the Si crystal is increased to 40 nm the visibility decreases for all Sr positions and the Sr atoms remains visible only up to a displacement

of  $\sim 0.3 \text{ \AA}$  in HAADF.

In order to understand the role of channeling, the multislice simulations are compared with a much simpler model, which does not take into account the evolution of the probe in the sample, but is simply the convolution of the incident probe intensity with the projected position of all the atoms in the sample weighted by  $Z^{1.7}$ . In this simple model, in which channeling is ignored, the visibility of an on-column Sr atom is reduced as expected. In addition we find that the visibility falls off more gradually with the displacement of the Sr atom. This suggests that electron channeling enhances the visibility of on-column atoms and filters out atoms that are sitting in-between the atomic columns. The rapid decrease in the visibility with Sr displacement can be understood by looking back at the evolution of the probe shape in the sample, discussed in section III A. As the probe channels in the crystal it narrows up and the intensity away from the atomic column decreases which in return results in a decrease in the visibility of an off-column atom. For HAADF imaging the Sr visibility therefore closely follows the probe shape after propagation through 10 nm of Si (Fig. 7).

After displacing the Sr atom by  $2.715 \text{ \AA}$  along a  $\langle 100 \rangle_{Si}$  direction it is again aligned with a Si atomic column, however, now the Sr atom is much closer to the last Si atom in that column. In the simple model, only the projected positions of all the atoms in the sample matter and the visibility is, therefore, for both Sr positions the same. The multislice results show, however, that the reduction in the distance between the last Si atom in the column and the Sr atom causes an increase in the Sr visibility. In LAADF imaging of a 10 nm thick Si crystal the visibility of a single Sr atom approaches 2.

Finally, the multislice simulations also predict an increase in the visibility as the detector angles are changed from HAADF to LAADF imaging (Fig. 7), which explains why we have used LAADF imaging conditions in the experimental setup.

The results discussed above imply that channeling in a crystal can be used not only to enhance the visibility of a thin layer, but also as a filter for imaging on-column atoms. If, on the other hand, one tries to also image off-column atoms, channeling is not desirable.

For the a-Si/SrTiO<sub>3</sub>/Si sample one option is to flip the sample up-side-down, so that the a-Si constitutes the entrance surface. In that case, channeling occurs after the probe has scattered off the SrTiO<sub>3</sub> layer and, hence, all atoms in the thin SrTiO<sub>3</sub> layer are imaged. In Fig. 8 LAADF images of a a-Si/SrTiO<sub>3</sub>/Si sample for the two orientations, Si substrate on top (Fig. 8(a)) and a-Si on top (Fig. 8(b)), are compared. For clarity, we have chosen a sample where the thickness of the Sr template was increased to 1 ML, which results in a lower density of SrTiO<sub>3</sub> islands when imaged using channeling in the Si substrate. Figure 8 shows that the apparent coverage increases from  $\sim 30\%$  to  $\sim 55\%$ , when the sample is imaged in the “a-Si on the top” geometry. When imaged

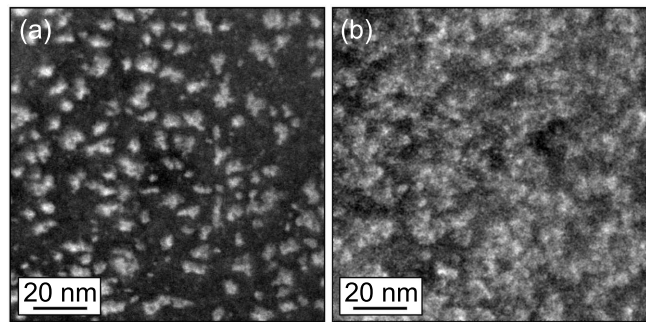


FIG. 8: Plan-view ADF-STEM images of a nominally 2.5 uc thick epitaxial SrTiO<sub>3</sub>(100) film grown on Si(100) using a 1 ML thick Sr template and capped with 15 nm of amorphous Si viewed along a substrate  $\langle 001 \rangle$  zone axis. The sample is oriented so that (a) the Si substrate and (b) the a-Si layer constitutes the entrance surface. When electron channeling is used to enhance the visibility of the SrTiO<sub>3</sub> layer, the SrTiO<sub>3</sub> that is aligned with the Si columns is preferentially imaged and the apparent coverage decreases.

through the Si substrate, the visibility of the SrTiO<sub>3</sub> islands is enhanced due to channeling in the crystal, but Sr atoms that are sitting off-column are filtered out. This suggests that  $\sim 45\%$  of the SrTiO<sub>3</sub> is sitting between the Si columns.

Using this channeling method SrTiO<sub>3</sub> islands that are coherent with the substrate can therefore be distinguished from relaxed SrTiO<sub>3</sub>. The fraction of coherent islands in epitaxial SrTiO<sub>3</sub>/Si is strongly dependent on the growth method. The SrTiO<sub>3</sub> films imaged here formed in a topotactic reaction on Si(100), as described in the experimental section. By choosing growth conditions away from equilibrium, in which the SrTiO<sub>3</sub> is not recrystallized from an amorphous state<sup>11,12,31</sup>, the fraction of coherent SrTiO<sub>3</sub> islands can be increased<sup>11</sup>.

#### IV. SUMMARY AND CONCLUSIONS

Electron channeling effects in the Si substrate have been exploited to image thin, buried epitaxial SrTiO<sub>3</sub> layers in plan-view ADF-STEM<sup>11</sup>. Here, we have used the same sample to directly measure the changes in the electron channeling signal with thickness of the Si substrate by tracking the increase in the ADF intensity due to the presence of thin SrTiO<sub>3</sub> islands. Multislice simulations of channeling in Si(100) agree with the experimental results when phonon scattering is taken into account.

At a thickness of 12 nm the channeling signal reaches its maximum at which the intensity of the SrTiO<sub>3</sub> islands has increased fourfold. This enhancement in the visibility of the islands is lost when the sample is flipped up-side-down and channeling occurs only after the electron probe has scattered off the SrTiO<sub>3</sub> layer. In that case, the contribution to the ADF intensity due to the presence of SrTiO<sub>3</sub> islands remains constant as the thickness of

the substrate is increase by moving to a thicker part of the wedge-shaped sample.

Using the multislice method we have further shown that while channeling results in an increase in the visibility of on-column atoms, it suppresses the contrast from Sr atoms sitting between the Si atomic columns. It therefore acts as a filter for on-column atoms and should be avoided if it is desired to also image atoms between the atomic columns of the substrate.

## Acknowledgments

The work at Cornell (L.F.K., M.K.P., D.G.S., D.A.M.) was supported by the Cornell Center for Materials Research (NSF No. DMR-0520404 and No. IMR-0417392) with additional support from the Office of Naval Research through grant N00014-04-1-0426 monitored by Colin Wood..

- 
- \* [lf56@cornell.edu](mailto:lf56@cornell.edu)
- <sup>†</sup> Current address: Department of Geology and Geophysics, Yale University, New Haven, CT 06520
- <sup>‡</sup> Current address: MEMC Electronic Materials, Inc., St. Peters, MO 63376
- <sup>1</sup> A. Ohtomo, D. A. Muller, J. L. Grazul, and H. Y. Hwang, *Nature* **419**, 378 (2002).
  - <sup>2</sup> D. A. Muller, N. Nakagawa, A. Ohtomo, J. L. Grazul, and H. Y. Hwang, *Nature* **430**, 657 (2004).
  - <sup>3</sup> M. M. McGibbon, N. D. Browning, M. F. Chisholm, A. J. McGibbon, S. J. Pennycook, V. Ravikumar, V. P. Dravid, *Science* **266**, 102 (1994).
  - <sup>4</sup> Z. Zhang, W. Sigle, M. Rühle, *Phys. Rev. B* **66**, 214112 (2002).
  - <sup>5</sup> A. Howie, *J. Microsc.* **117**, 11 (1979).
  - <sup>6</sup> E. J. Kirkland, R. F. Loane, and J. Silcox, *Ultramicroscopy* **23**, 77 (1987).
  - <sup>7</sup> J. Fertig, and H. Rose, *Optik* **59**, 407 (1981).
  - <sup>8</sup> R. F. Loane, E. J. Kirkland, and J. Silcox, *Acta Crystallogr. Sect. A* **44**, 912 (1988).
  - <sup>9</sup> J. M. Cowley, J. C. H. Spence, and V. V. Smirnov, *Ultramicroscopy* **68**, 135 (1997).
  - <sup>10</sup> P. M. Voyles, J. L. Grazul, D. A. Muller, *Ultramicroscopy* **96**, 251 (2003).
  - <sup>11</sup> L. Fitting Kourkoutis, C. S. Hellberg, V. Vaithyanathan, H. Li, M. K. Parker, K. E. Andersen, D. G. Schlom, D. A. Muller, *Phys. Rev. Lett.* **100**, 036101 (2008).
  - <sup>12</sup> H. Li, X. Hu, Y. Wei, Z. Yu, X. Zhang, R. Droopad, A. A. Demkov, J. Edwards, K. Moore, W. Ooms, J. Kulik, and P. Fejes, *J. Appl. Phys.* **93**, 4521 (2003).
  - <sup>13</sup> J. Lettieri, Ph.D. thesis, Pennsylvania State University (2002). Available online at <http://etda.libraries.psu.edu/theses/approved/WorldWideIndex/ETD-202/index.html>.
  - <sup>14</sup> Y. Liang, S. Gan, and M. Engelhard, *Appl. Phys. Lett.* **79**, 3591 (2001).
  - <sup>15</sup> J. Lettieri, J. H. Haeni, and D. G. Schlom, *J. Vac. Sci. Technol. A* **20**, 1332 (2002).
  - <sup>16</sup> L. V. Goncharova, D. G. Starodub, E. Garfunkel, T. Gustafsson, V. Vaithyanathan, J. Lettieri, and D. G. Schlom, *J. Appl. Phys.* **100**, 14912 (2006).
  - <sup>17</sup> M. Weyland, and D. A. Muller, *FEI, Nano Solution* **1**, 24 (2005).
  - <sup>18</sup> J. M. Cowley, and A. F. Moodie, *Acta Cryst.* **10**, 609 (1957).
  - <sup>19</sup> P. Goodman, and A. F. Moodie, *Acta Cryst.* **A30**, 280 (1974).
  - <sup>20</sup> E. J. Kirkland, *Advanced Computing in Electron Microscopy*. New York: Plenum.
  - <sup>21</sup> R. F. Loane, P. Xu, and J. Silcox, *Acta Cryst. A* **47**, 267 (1991).
  - <sup>22</sup> S. E. Hillyard, and J. Silcox, *Ultramicroscopy* **58**, 6 (1995).
  - <sup>23</sup> D. A. Muller, B. Edwards, E. J. Kirkland, and J. Silcox, *Ultramicroscopy* **86**, 371 (2001).
  - <sup>24</sup> P. Xu, R. F. Loane, and J. Silcox, *Ultramicroscopy* **38**, 127 (1991).
  - <sup>25</sup> J. M. Cowley, *Ultramicroscopy* **4**, 435 (1979).
  - <sup>26</sup> J. M. LeBeau, S. D. Findlay, X. Wang, A. J. Jacobson, L. J. Allen, S. Stemmer, *Phys. Rev. B* **79**, 214110 (2009).
  - <sup>27</sup> J. M. LeBeau, S. D. Findlay, L. J. Allen, S. Stemmer, *Ultramicroscopy* **110**, 118 (2010).
  - <sup>28</sup> R. F. Loane, P. Xu, and J. Silcox, *Ultramicroscopy* **40**, 121 (1992).
  - <sup>29</sup> J. P. Langmore, J. Wall, and M. S. Isaacson, *Optik* **38**, 335 (1973).
  - <sup>30</sup> Z. Yu, D. A. Muller, J. Silcox, *J. Appl. Phys.* **95**, 3362 (2004).
  - <sup>31</sup> M. P. Warusawithana, C. Cen, C. R. Slesman, J. C. Woicik, Y. Li, L. Fitting Kourkoutis, J. A. Klug, H. Li, P. Ryan, L.-P. Wang, M. Bedzyk, D. A. Muller, L.-Q. Chen, J. Levy, D. G. Schlom, *Science* **324**, 367 (2009).